Modeling Water-Mass Distributions in the Modern and LGM Ocean: Circulation Change and Isopycnal and Diapycnal Mixing

C. S. JONES[a] AND RYAN P. ABERNATHEY[a]

[a] *Lamont–Doherty Earth Observatory, Palisades, New York*

(Manuscript received 19 August 2020, in final form 28 January 2021)

ABSTRACT: Paleoproxy observations suggest that deep-ocean water-mass distributions were different at the Last Glacial Maximum than they are today. However, even modern deep-ocean water-mass distributions are not completely explained by observations of the modern ocean circulation. This paper investigates two processes that influence deep-ocean water-mass distributions: 1) interior downwelling caused by vertical mixing that increases in the downward direction and 2) isopycnal mixing. Passive tracers are used to assess how changes in the circulation and in the isopycnal-mixing coefficient impact deep-ocean water-mass distributions in an idealized two-basin model. We compare two circulations, one in which the upper cell of the overturning reaches to 4000-m depth and one in which it shoals to 2500-m depth. Previous work suggests that in the latter case the upper cell and the abyssal cell of the overturning are separate structures. Nonetheless, high concentrations of North Atlantic Water (NAW) are found in our model's abyssal cell: these tracers are advected into the abyssal cell by interior downwelling caused by our vertical mixing profile, which increases in the downward direction. Further experiments suggest that the NAW concentration in the deep South Atlantic Ocean and in the deep Pacific Ocean is influenced by the isopycnal-mixing coefficient in the top 2000 m of the Southern Ocean. Both the strength and the vertical profile of isopycnal mixing are important for setting deep-ocean tracer concentrations. A 1D advection–diffusion model elucidates how NAW concentration depends on advective and diffusive processes.

KEYWORDS: Mesoscale processes; Mixing; Ocean circulation; Ocean dynamics; Transport; Paleoclimate

1. Introduction

Ocean water-mass distributions are influenced by the large-scale ocean circulation, isopycnal and diapycnal mixing. This paper explores how each of these mechanisms affects deep-ocean water-mass distributions, with a focus on comparing scenarios representative of the modern ocean and the Last Glacial Maximum (LGM). In this introduction, we summarize current understanding of the processes that determine deep-ocean water-mass distributions during these two time periods and show some places where there are gaps in this understanding.

The modern ocean overturning circulation is often described as a figure-eight loop, in which North Atlantic Deep Water (NADW) is formed in the North Atlantic Ocean, flows southward in the deep Atlantic, and upwells in the Southern Ocean, where it is ventilated at the surface, gaining new water-mass characteristics before it sinks to form Antarctic Bottom Water (AABW). This AABW flows northward in the abyssal Pacific Ocean before surfacing and returning to the North Atlantic at surface and intermediate depths (Talley 2013).

A variety of proxy measurements indicate that the fraction of water in the deep Atlantic that originated at the surface of the North Atlantic was reduced at the LGM (Lynch-Stieglitz et al. 2007; Curry and Oppo 2005; Gebbie 2014; Howe et al. 2016; Oppo et al. 2018). Adkins (2013) and Ferrari et al. (2014) suggested that the maximum depth of North Atlantic Water (NAW) shoaled during the LGM and that the figure-eight loop associated with the modern overturning circulation was split into two largely unconnected cells: an upper cell that comprised sinking in the North Atlantic and upwelling elsewhere, and an abyssal cell that comprised sinking in the Southern Ocean and upwelling elsewhere.

Marzocchi and Jansen (2019) found that, in a single-basin ocean model, the abyssal cell of the overturning was more isolated under global atmospheric cooling, both because shoaling of the interface between the upper and abyssal cells leads to a weaker downward mixing of North Atlantic Water and because increased sea ice around Antarctica inhibits air–sea gas exchange (Stephens and Keeling 2000). Increased isolation of the abyssal cell leads to more carbon storage in the deep ocean, which is one possible cause of reduced atmospheric CO_2 levels at the LGM (Watson et al. 2015; Ferreira et al. 2018; Nadeau et al. 2019; Marzocchi and Jansen 2019).

Not all models agree that the upper cell shoaled at the LGM. Sun et al. (2018) showed that diapycnal mixing in the Southern Ocean reduces the influence of Southern Ocean buoyancy forcing on isopycnal depth in the Atlantic basin. Additionally, because the mean sea level was lower at the LGM, increased tidal dissipation may have boosted diapycnal mixing, which may actually cause North Atlantic Water to sink to deeper depths in the North Atlantic (Wilmes et al. 2019).

Based on proxy observations, it is unclear how isolated the abyssal cell became at the LGM. The nonconservative nature of nutrient-based tracers (e.g., $\delta^{13}C$) leads to uncertainty in these proxy estimates of the fraction of North Atlantic Water in the deep Atlantic Ocean during the LGM. Using

Supplemental information related to this paper is available at the Journals Online website: https://doi.org/10.1175/JPO-D-20-0204.s1.

Corresponding author: C. Spencer Jones, spencerj@ldeo.columbia.edu

DOI: 10.1175/JPO-D-20-0204.1

neodymium isotopes, which are independent of biological processes, Howe et al. (2016) found only a modest reduction in the amount of North Atlantic Water in the deep Atlantic at the LGM: this is consistent with more recent nutrient-based estimates by Gebbie (2014) and Oppo et al. (2018) that use multiple tracers to reduce uncertainties.

Previous work that assumed the two overturning cells were separated at the LGM did not examine mechanisms for North Atlantic Water to reach the abyssal cell. One possible way for North Atlantic Water to enter the abyssal ocean is through interior downwelling. Ferrari et al. (2016) recently found that, for a profile of vertical diffusivity that increases toward the bottom of the ocean, consistent with modern observational estimates (St. Laurent et al. 2012; Waterman et al. 2013; Waterhouse et al. 2014; Kunze 2017b), interior mixing drives downwelling across density surfaces. Ferrari et al. (2016) showed that this downwelling is compensated by upwelling at the same depth in the topographic boundary layer. Using hydrographic observations of the modern ocean, Kunze (2017a) inferred downward diapycnal velocities between NADW and AABW in the modern Atlantic ocean. How North Atlantic Water reaches the deep ocean is not well understood, and it is unclear whether interior downwelling is an important pathway for tracers to enter the deep ocean below 2000 m (Mashayek et al. 2017).

Isopycnal mixing also influences deep-ocean tracer concentrations. Mesoscale eddies, which have scales of about 100 km, are not resolved in coarse-resolution ocean and climate models, which usually have resolutions of around 1°. Instead, the subgrid-scale eddy tracer fluxes are represented using the Gent and McWilliams (1990) and Redi (1982) schemes. The Redi (1982) scheme parameterizes the diffusive part of eddy transport using a diffusion operator that acts in the isopycnal direction, multiplied by an isopycnal-mixing coefficient. Observational studies give a wide range of values for this isopycnal-mixing coefficient, from 10 to 10 000 $m^2 s^{-1}$ (Groeskamp et al. 2017; Armi and Stommel 1983; Ledwell et al. 1998; Garabato et al. 2007; Tulloch et al. 2014; Lumpkin and Speer 2007; Cole et al. 2015; Roach et al. 2018; Rudnickas et al. 2019). This wide range of values is partly caused by regional variations in the strength of isopycnal mixing, but the size of the isopycnal-mixing coefficient is still very uncertain.

Isopycnal mixing has a strong influence on ocean tracer distributions (Trossman et al. 2012; Abernathey and Ferreira 2015; Gnanadesikan et al. 2015; Burke et al. 2015; Kamenkovich et al. 2017; Jones and Abernathey 2019; Ragen et al. 2020; Pavia et al. 2020). In a high-resolution model of the Southern Ocean, Abernathey and Ferreira (2015) showed stronger winds drive stronger eddies, leading to more isopycnal mixing. Some evidence suggests that winds over the Southern Ocean were more powerful at the LGM than they are today, and that the southern westerly wind jet may have shifted northward or southward from its current position (Stuut et al. 2002; Kim et al. 2003; Kohfeld et al. 2013; Gottschalk et al. 2019). Climate models from the Paleoclimate Modeling Intercomparison Project (PMIP) do not consistently show such a change. PMIP models show a maximum increase in wind strength of about 40%, but do not rule out more extreme wind changes at the LGM (Sime et al. 2013; Rojas 2013; Sime et al. 2016).

If Southern Ocean winds were stronger at the LGM, isopycnal mixing in the Southern Ocean may also have been stronger. Research that interprets proxy observations of LGM tracer distributions typically neglects this possibility, focusing on changes in the ocean circulation at the LGM. Ocean observations suggest that the isopycnal mixing coefficient is higher in the surface ocean than in the deep ocean (Cole et al. 2015; Roach et al. 2018), and modeling shows that the isopycnal mixing coefficient in the top 2000 m is sensitive to wind stress (Abernathey and Ferreira 2015).

The studies above indicate that the overturning circulation, diapycnal mixing, and interior isopycnal mixing may help determine the composition of deep waters. But there is no clear consensus on the relative importance of the different mechanisms, nor how they changed between the modern and LGM oceans. To address this gap in knowledge, here we study the problem using idealized simulations and, where possible, a simple theoretical model. We hope that our results will enable more complete interpretation of LGM paleoproxy measurements in the future.

2. 3D primitive equation model

In this section, we assess how changes to the circulation and to the isopycnal-mixing coefficient affect deep-ocean tracer distributions, by varying these properties in a 3D primitive equation model. The idealized geometry of the model enables us to characterize individual transport processes more easily. Using this model, we examine the pathways of North Atlantic Water in two different circulation regimes and investigate the effects of vertical variations in the isopycnal-mixing coefficient on tracer distributions.

The Massachusetts Institute of Technology general circulation model (MITgcm; Marshall et al. 1997) is configured to model the global ocean in an idealized-geometry two-basin domain like the one used in Jones and Abernathey (2019). It is a spherical sector, with 1° resolution, that spans from 70°S to 70°N and 210° in longitude. Two one-gridpoint-wide continents, which run in the meridional direction, divide the domain into a narrow basin that represents the Atlantic and a wide basin that represents the Pacific. The continent to the west of the Atlantic basin, which represents the Americas, runs from 52.5°S to 70°N. South of this continent is a ridge of height 1333 m and a short wall that represents the Antarctic Peninsula and extends from 70° to 65°S. The continent to the east of the Atlantic, which represents Africa/Asia, extends from 35°S to 70°N. A Mercator projection of the domain is shown in Fig. 1d. The domain was chosen for its simplicity, which allows the model to capture the main features of the meridional overturning circulation without the complexities associated with detailed topography and enables easy comparison with the 1D advection–diffusion model described in section 4.

Except in the crosshatched area near the southern boundary in Fig. 1d, the model is forced at the surface with zonally uniform zonal wind stress, temperature relaxation and freshwater flux, which are shown in Figs. 1a–c. Even though this forcing is zonally uniform, deep water is formed in the North Atlantic

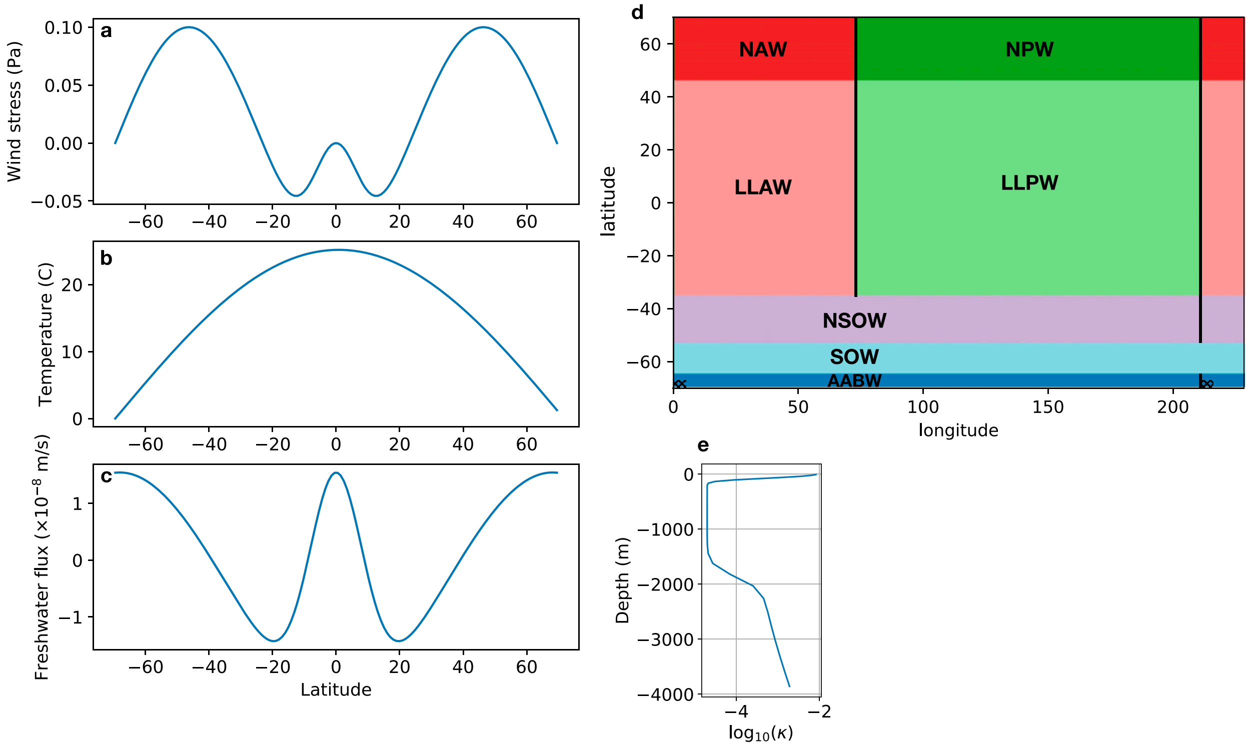

FIG. 1. (a) Surface wind stress (Pa), (b) surface temperature relaxation profile (°C), and (c) surface freshwater flux ($\times 10^{-8}\,\mathrm{m\,s^{-1}}$). (d) Surface regions associated with each of the passive tracers. The concentration of each tracer is relaxed to one in its associated surface region and to zero at the surface outside this region. The westernmost 20° of the domain is repeated to the right of the figure. In the small cross-hatched region at 70°S and 0°, and repeated at 70°S and 210°E, the surface freshwater flux is set to $-2 \times 10^{-7}\,\mathrm{m\,s^{-1}}$ for the modern ocean and $-2.4 \times 10^{-6}\,\mathrm{m\,s^{-1}}$ for the shoaled upper cell to simulate a polynya. (e) The original vertical diffusivity profile, used for temperature and salinity in all of the experiments shown here.

and not in the North Pacific, as detailed in Jones and Cessi (2017).

In the crosshatched area, the freshwater flux has a uniform value of $-2 \times 10^{-7}\mathrm{m\,s^{-1}}$ for the modern ocean, and the temperature is relaxed to 0°C. This high negative freshwater flux represents brine rejection, and the crosshatched area represents a coastal polynya. In some experiments, the freshwater flux in this area is reduced to $-2.4 \times 10^{-6}\,\mathrm{m\,s^{-1}}$ to achieve a shoaled-upper-cell (SUC) circulation similar to that described by Ferrari et al. (2014).[1] A small constant is added to the freshwater flux to ensure that the net freshwater flux into the whole domain is zero.

We choose a linear equation of state, which enables clear attribution of the vertical velocities described later in the paper. The buoyancy b is given by

$$b = g[\alpha T - \beta(S - S_{\mathrm{ref}})]\,, \tag{1}$$

where $\alpha = 2 \times 10^{-4}\,°\mathrm{C}^{-1}$, $\beta = 7.4 \times 10^{-4}$, $g = 9.81\,\mathrm{m^2\,s^{-1}}$, and $S_{\mathrm{ref}} = 35$. Salinity S is given on the practical salinity scale and is therefore presented without units. Temperature T is in degrees Celsius. The Gent–McWilliams coefficient is set to $500\,\mathrm{m^2\,s^{-1}}$ in all simulations.

Our experiments use a vertical diffusivity profile of

$$\kappa = \kappa_v + \{\kappa_{\mathrm{deep}} + \kappa_{\mathrm{abyss}}[10^{-(z+4000)/2000}]\} \times \frac{\left[1 - \tanh\left(\dfrac{z+2000}{200}\right)\right]}{2} + 10^{-2}\frac{\left[1 + \tanh\left(\dfrac{z+30}{30}\right)\right]}{2}\,. \tag{2}$$

This represents a high-diffusivity mixed layer above 30-m depth, below which the vertical diffusivity tapers to κ_v, increasing to $\kappa_{\mathrm{deep}} + \kappa_v$ at 2000 m and $\kappa_{\mathrm{abyss}} + \kappa_{\mathrm{deep}} + \kappa_v$ near the bottom. For temperature and salinity, $\kappa_v = 2 \times 10^{-5}\,\mathrm{m^2\,s^{-1}}$, $\kappa_{\mathrm{deep}} = 2 \times 10^{-4}\,\mathrm{m^2\,s^{-1}}$, and $\kappa_{\mathrm{abyss}} = 2 \times 10^{-3}\,\mathrm{m^2\,s^{-1}}$. This vertical diffusivity (see Fig. 1e) profile is similar to that used by Nadeau et al. (2019). This profile is very idealized but emulates an increase in vertical mixing below 2000-m depth that is seen in observations (Nikurashin and Ferrari 2013). The vertical diffusivity profile for temperature and salinity is used for all tracers in the experiments below unless otherwise specified.

To trace where water was last ventilated, the model includes seven idealized water-mass tracers, each of which is associated

[1] In Ferrari et al. (2014), the expanded area of buoyancy loss at the LGM causes shoaling, but Jansen and Nadeau (2016) show that increasing the size of the buoyancy loss has a similar effect on the depth of the upper cell.

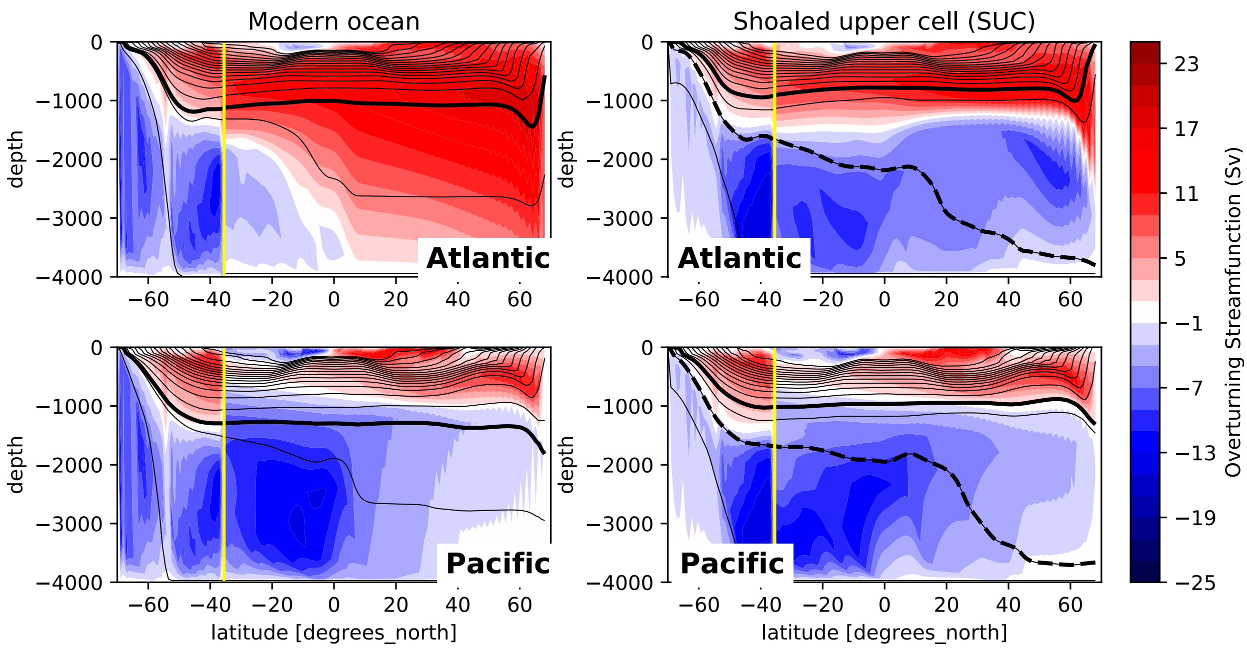

FIG. 2. Residual overturning streamfunction (colors; contour interval of 2 Sv), as defined in Eq. (3), transformed into z space using Eq. (4) and the zonally averaged depth of buoyancy surfaces (thin black contours; contour interval of 0.002 m^2 s^{-1}) in the (top) Atlantic and (bottom) Pacific for (left) the modern ocean and (right) the shoaled upper cell. The vertical yellow line marks 35°S: south of this line the overturning streamfunction is calculated over the whole domain rather than over each basin. The thick black solid contour shows the isopycnal b_m, which approximately divides the northward-flowing water in the Atlantic's upper cell from the southward-flowing water in the Atlantic's upper cell. The thick dashed contour shows isopycnal $b = 0.01$ m^2 s^{-1}, which defines the upper surface of layer 2 in the two-layer version of the 1D model.

with a region of the surface ocean as shown in Fig. 1d. Each tracer is relaxed to one at the surface inside its corresponding region and is relaxed to zero at the surface outside its corresponding region. Hence, in equilibrium the concentration of a tracer at any grid point in the domain indicates what fraction of water at that grid point was last ventilated in that tracer's corresponding region.

In some of the experiments shown here, the isopycnal-mixing coefficient for these idealized water-mass tracers, $\kappa_{\mathrm{redi}}^{\mathrm{tr}}$, is varied. The isopycnal-mixing coefficient for temperature and salinity is held constant at 500 m^2 s^{-1}. Hence the advective circulation does not change when $\kappa_{\mathrm{redi}}^{\mathrm{tr}}$ is modified.

The overturning for the modern and SUC experiments is shown in Fig. 2. This overturning is calculated in density space using

$$\psi(\tilde{y}, b) \equiv \frac{1}{T}\int_0^T \int_{x_w}^{x_e} \int_{-H}^{0} v\mathscr{H}[b(x, y, z, t) - \tilde{b}]dz\,dx\,dt, \qquad (3)$$

where v is the Eulerian plus parameterized eddy velocity, H is the total depth, x_e is the eastern edge of the basin, x_w is the western edge of the basin, T is the averaging time scale (100 years is chosen here), and $\mathscr{H}$ is the Heaviside function. The coordinates $(\tilde{t}, \tilde{x}, \tilde{y}, \tilde{z})$ represent (t, x, y, z) in buoyancy space rather than depth space, as described by Young (2012). The residual overturning streamfunction ψ is the zonally integrated transport of water above $b = \tilde{b}$. The streamfunction in density space is transformed back into depth space using zonal-mean isopycnal height,

$$\mathscr{Z}(\tilde{y}, b) \equiv -\frac{1}{T}\int_0^T \frac{1}{x_e - x_w}\int_{x_w}^{x_e} \int_{-H}^{0} \mathscr{H}\left[b(x, y, z, t) - \tilde{b}\right] dz\,dx\,dt. \qquad (4)$$

For ease of comparison with other models and paleoproxies, the overturning streamfunction calculated in depth coordinates is provided in the online supplemental material, and the tracer distributions shown below in Figs. 3–8 are zonally and time-averaged in depth space rather than in density space.

In the modern simulation, our model forms 20 Sv (1 Sv ≡ 10^6 m^3 s^{-1}) of deep water in the upper cell, consistent with estimates of NADW formation by Lumpkin and Speer (2007) and Talley (2013). This water sinks to a depth of 4000 m, the very bottom of our model domain. About 13 Sv of bottom water flows northward across 30°S: 10 Sv of this flows into the Pacific and 3 Sv flows into the Atlantic. As explained in Jones and Abernathey (2019), our model forms less bottom water than the real ocean, partly because our model has a smaller area. In addition, our domain only extends to 4000-m depth, so slightly less AABW enters the deep Atlantic in our model than in observations of the modern ocean.

In the SUC simulation, our model forms 15 Sv of North Atlantic Water in the upper cell, and about 17 Sv of bottom water flows northward across 30°S. The upper cell only reaches

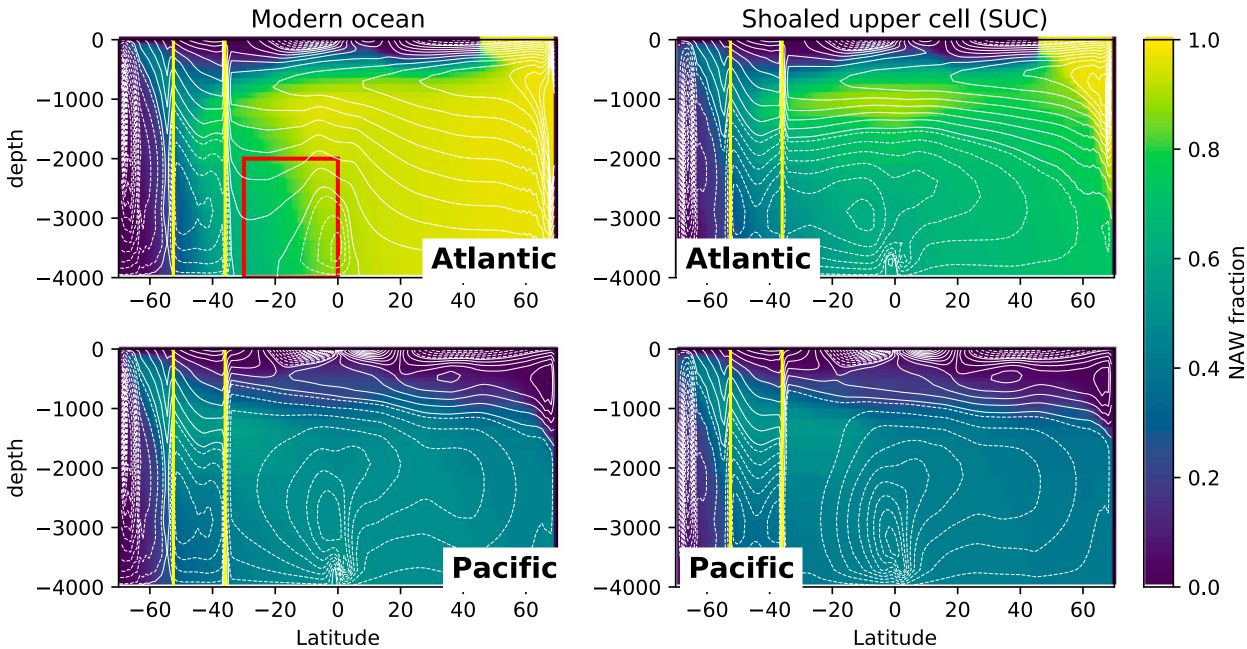

FIG. 3. NAW tracer concentration (colors), zonally averaged in depth space in the (top) Atlantic and (bottom) Pacific for (left) the modern ocean and (right) the shoaled upper cell. The vertical yellow lines at 35° and 52.5°S indicate where the short and long continents end, respectively. The white contours show the meridional overturning streamfunction calculated in depth space. North of 35°S the streamfunction is calculated for each basin, and south of 35°S it is calculated for the whole zonal extent of the domain. The red-outlined box in the top-left panel shows the volume used for averaging in Fig. 4.

to about 2500-m depth in the zonal average. The abyssal cell only has a strength of about 3 Sv in the Southern Ocean (Fig. 2), so our simulations may underestimate the role of advection in that region. The SUC simulation is also slightly more stratified than the modern simulation. There is some limited evidence that the LGM ocean was indeed more stratified than the modern ocean (Adkins et al. 2002; Lund et al. 2011).

3. Results of the 3D simulations

a. Comparing modern and SUC tracer distributions

In our first experiment, the isopycnal mixing coefficient for tracers, $\kappa_{\text{redi}}^{\text{tr}}$, is set to $500\,\text{m}^2\,\text{s}^{-1}$, equal to the isopycnal mixing coefficient for temperature and salinity. Only the circulation is varied. The concentration of the NAW tracer, which represents water originating at the surface of the North Atlantic, is shown in Fig. 3 for the modern and SUC ocean circulations. Shoaling the Atlantic's upper cell leads to a significant reduction in how much NAW reaches the deep Atlantic Ocean, and to a small decrease in how much NAW reaches the deep Pacific Ocean.

For our modern ocean circulation, close to 100% of water in the deep North Atlantic originates at the surface of the North Atlantic (top-left panel of Fig. 3). Our model slightly overestimates the amount of North Atlantic Water reaching the deep Atlantic when compared with modern observations by Johnson (2008). Because of the limited depth of our domain, the model underestimates the amount of AABW that enters the modern Atlantic Ocean. However, we do not expect this to qualitatively affect our results.

Figure 4 shows the mean water-mass tracer concentrations in the deep Atlantic between 30°S and the equator in several of our experiments. The SUC concentration of NAW tracer for $\kappa_{\text{redi}}^{\text{tr}} = 500\,\text{m}^2\,\text{s}^{-1}$ in the deep Atlantic between 30°S and the equator is about 0.65, which is approximately consistent with LGM observations by Howe et al. (2016) and Oppo et al. (2018). In our model, NADW concentrations above 0.8 persist into the Southern Hemisphere and are concentrated around 1200 m depth. This high peak is not seen in the observations: this could be caused by the sparseness of data available, but it could also indicate that large-scale circulation change is not the only mechanism that caused changes in water-mass distributions at the LGM.

Given that the upper and abyssal cells of the overturning circulation appear to be totally separate in Fig. 2, *it is somewhat surprising that the abyssal Atlantic is not composed entirely of Southern Ocean water*. We would therefore like to understand how North Atlantic Water enters the abyssal cell for our shoaled-upper-cell circulation. In observations and in models with realistic sea ice, air–sea gas exchange is inhibited in areas with high sea ice concentrations. Hence in models with sea ice, North Atlantic Water that passes close to the surface under sea ice generally retains some of its properties as it sinks in the abyssal cell (Nadeau et al. 2019). Our idealized model does not include sea ice at the surface, so in the mixed layer of the Southern Ocean, the concentration of NAW tracer is close to zero. Therefore, for North Atlantic surface waters to enter the

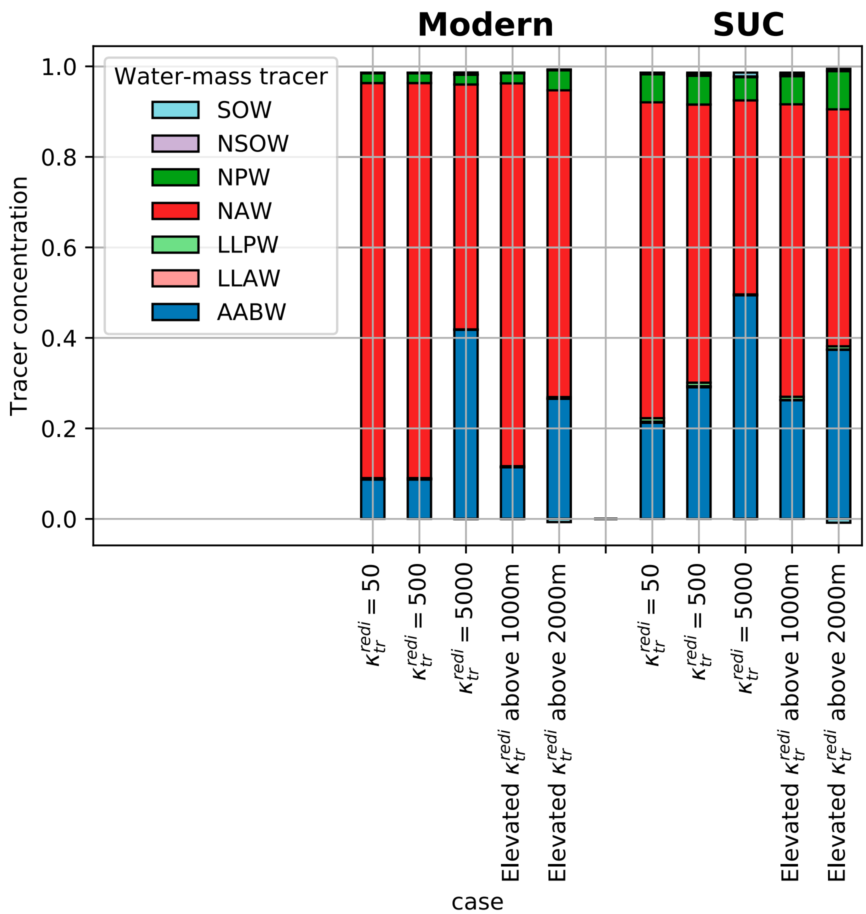

FIG. 4. Concentration of the seven water-mass tracers shown in Fig. 1d in Atlantic Ocean between 30°S and 0° and below 2000 m (see also the red-outlined box in Fig. 3) in 10 of the experiments, shown here.

deep Atlantic Ocean, they must not reach the mixed layer of the Southern Ocean at all. For the SUC, North Atlantic Water cannot enter the abyssal Atlantic by isopycnal diffusion alone, because the deep Atlantic is much denser than the surface North Atlantic. Instead *NAW tracer must enter the abyssal cell away from the mixed layer*, either by advection or by vertical diffusion.

To clarify how North Atlantic Water reaches the abyssal cell in the SUC state, we want to test whether vertical diffusion is transporting North Atlantic Water into the abyssal cell. We reduce the vertical diffusivity used to transport the water-mass tracers, κ_v^{tr}, to a constant value of $2 \times 10^{-5}\,\mathrm{m^2\,s^{-1}}$ below the mixed layer ($\kappa_{\rm deep}^{tr} = \kappa_{\rm abyss}^{tr} = 0$). Note that because the change in κ_v^{tr} is applied to the passive tracers, not to temperature and salinity, the velocities in this simulation remain the same as before. They are still controlled by the original vertical diffusivity profile, which increases toward the bottom of the ocean.

The concentration of the NAW tracer for this simulation is shown in Fig. 5. The vertical diffusivity for water-mass tracers is very small in this experiment, but about 40% of the water in the abyssal Atlantic still originates at the surface of the North Atlantic. This result strongly suggests that significant amounts of North Atlantic Water are advected from the upper cell into the abyssal cell in our SUC state.

To characterize advection from the upper cell to the abyssal cell, we plot the zonally integrated diapycnal transport in the Atlantic in Fig. 6. We estimated the diapycnal transport from the divergence of the isopycnal volume transport in density coordinates, which we obtain from the MITgcm's layers package. For the modern ocean circulation, there is significant diapycnal transport toward higher densities south of the equator (Fig. 6a), with about 7 Sv of downward volume transport at 2000-m depth (Fig. 6c). For the SUC, there is significant diapycnal transport toward higher densities across most of the Atlantic (Fig. 6b), with about 4 Sv of downward transport across 2000 m between 36°S and the equator (Fig. 6c). For the SUC, the depth of this downwelling corresponds with the division between the two cells, so this downwelling is likely to transport NAW from the upper cell to the abyssal cell. These downward diapycnal velocities are qualitatively similar to those found by Kunze (2017a, see the top-right panel of his Fig. 6). Kunze (2017a) inferred these velocities from observationally derived maps of vertical diffusivity.

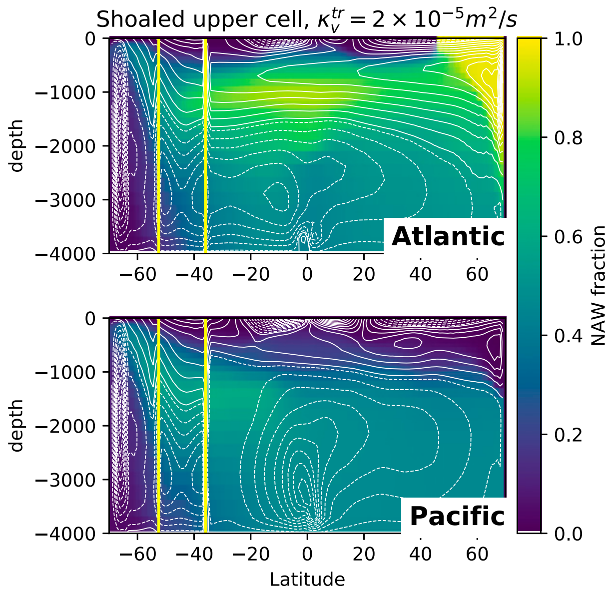

FIG. 5. NAW tracer concentration in the (top) Atlantic and (bottom) Pacific for the SUC circulation with $\kappa_v^{tr} = 2 \times 10^{-5}$ m^2 s^{-1}, with $\kappa_{deep}^{tr} = \kappa_{abyss}^{tr} = 0$. The vertical yellow lines at 35° and 52.5°S indicate where the short and long continents end, respectively. The white contours show the meridional overturning streamfunction calculated in depth space. North of 35°S the streamfunction is calculated for each basin, and south of 35°S it is calculated for the whole zonal extent of the domain. Note that the modified κ_v^{tr} acts on passive tracers only, so the velocity field in this experiment is the same as in all of the modern ocean experiments.

b. *Uniform changes to the isopycnal mixing coefficient*

The isopycnal-mixing coefficient may have been larger at the LGM. In this section, we assess whether an increase in the isopycnal-mixing coefficient could reduce the concentrations of NAW in the deep ocean, and whether the size of this reduction is significant relative to the reduction caused by a shoaling of the AMOC's upper cell. Figures 7a–d show the concentration of NAW tracer in the Atlantic basin in the modern ocean and for the SUC when $\kappa_{redi}^{tr} = 50$ m^2 s^{-1} and when $\kappa_{redi}^{tr} = 5000$ m^2 s^{-1}. Figures 7e and 7f show the difference between $\kappa_{redi}^{tr} = 5000$ m^2 s^{-1} and $\kappa_{redi}^{tr} = 50$ m^2 s^{-1} for the modern and SUC circulations.

Figure 7 shows that both shoaling the upper cell of the MOC and increasing the isopycnal-mixing coefficient reduce the concentration of North Atlantic Water in the deep Atlantic. Shoaling the upper cell affects Atlantic tracer concentrations north of the channel and below 1000-m depth. Changing the isopycnal mixing coefficient affects Atlantic tracer concentrations in the Southern Hemisphere more than it affects tracer concentrations in the Northern Hemisphere, and this Southern Hemisphere change is more pronounced in the upper cell of the overturning circulation.

Shoaling the upper cell reduces the deep Atlantic ocean NAW tracer concentration by about 0.15 for fixed κ_{redi}^{tr} (cf. red bars in Fig. 4). Increasing the isopycnal-mixing coefficient from $\kappa_{redi}^{tr} = 50$ m^2 s^{-1} to $\kappa_{redi}^{tr} = 5000$ m^2 s^{-1} has a larger effect on the deep ocean for the modern ocean circulation, and a smaller effect for a shoaled upper cell, but in both cases this effect has the same order of magnitude as the effect of changing the circulation.

c. *Nonuniform changes to the isopycnal mixing coefficient*

Observations show that the isopycnal-mixing coefficient is higher in the surface ocean than in the deep ocean (Cole et al. 2015; Roach et al. 2018). Hence, experiments in which the isopycnal mixing coefficient is uniform in depth are unrealistic. Next, we performed experiments in which the isopycnal-mixing coefficient for idealized tracers was only changed above a specific depth level d, according to

$$\kappa_{pr}(d) = 5000\left[0.505 + 0.495\tanh\left(\frac{z+d}{200}\right)\right]. \qquad (5)$$

In other words, κ_{redi}^{tr} was set to 5000 m^2 s^{-1} above d and was smoothly tapered to 50 m^2 s^{-1} below d.

In one of these experiments $d = 1000$ m, and in the other $d = 2000$ m. Figure 8 shows the concentration of NAW tracer in these two experiments relative to an experiment in which $\kappa_{redi}^{tr} = 50$ m^2 s^{-1}. When the isopycnal-mixing coefficient is boosted only above 1000 m, the effects on tracer distributions are mostly confined above 1000 m (Figs. 8b,c). When the isopycnal-mixing coefficient is boosted above 2000 m, NAW tracer concentrations decrease throughout the whole water column and particularly in the abyssal cell (Figs. 8e,f), even though there is no change to the isopycnal-mixing coefficient below 2000 m. This indicates that changes in the strength of isopycnal mixing in the top 2000 m can have a large impact on deep-ocean tracer distributions. This impact is similar to the impact of shoaling the upper cell (Fig. 4).

d. *Summary of results from the 3D model*

Figure 4 shows the concentration of each water-mass tracer in the Atlantic between 30°S and 0° and below 2000 m for most of the experiments we performed. This region is chosen because it is comparatively well sampled in proxy measurements of the LGM. Figure 4 shows that, for both modern and shoaled circulations, as isopycnal mixing is increased, the concentration of North Atlantic Water in the South Atlantic decreases, and that this water is replaced by AABW. Elevating the isopycnal mixing coefficient above 1000 m has basically no effect on tracer concentrations in the deep ocean, but elevating the isopycnal-mixing coefficient above 2000 m decreases the amount of North Atlantic Water and increases the amount of AABW tracer in the deep ocean.

4. 1D advection–diffusion model

The 3D model shows that isopycnal mixing above 2000 m is an important control on deep-ocean water-mass distributions, both today and at the LGM. However, it is not clear whether zonal correlations between velocity and tracer concentration impact tracer transport in the 3D experiments. In this section, we explore how different isopycnal mixing patterns affect deep-ocean tracer distributions using a 1D advection–diffusion

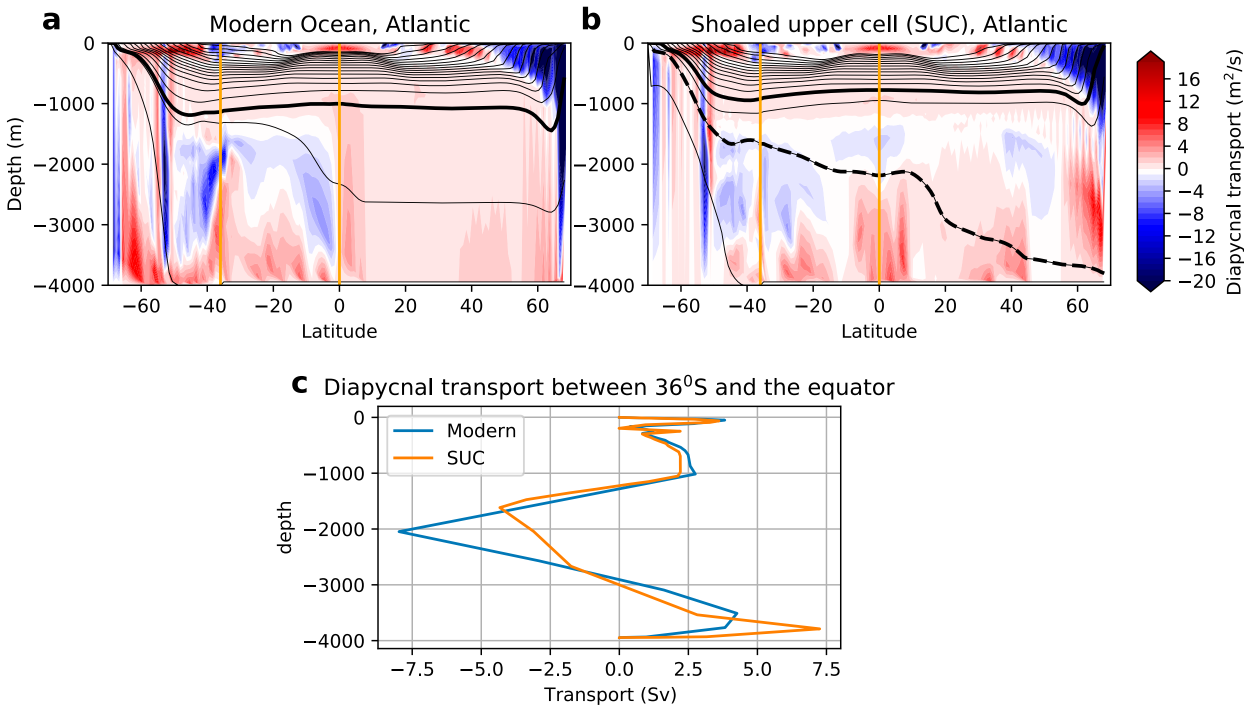

FIG. 6. Diapycnal velocity for (a) the modern ocean and (b) the shoaled upper cell, zonally integrated across the Atlantic and transformed into z space using Eq. (4). Vertical orange lines in (a) and (b) indicate 36°S and the equator. (c) The diapycnal transport between 36°S and the equator.

model. By eliminating many of the complexities of the 3D model, the 1D model clarifies the mechanisms that influence deep-ocean tracer concentrations when the isopycnal-mixing coefficient is changed.

a. Formulation of the 1D model

Initially, we set up this 1D model to predict tracer distributions below the dividing isopycnal b_m (the thick black contour in Fig. 2) by making various simplifying assumptions about tracer advection and diffusion. The isopycnal b_m is chosen because it passes through the maximum of the upper cell of the MOC, as in Jones and Cessi (2017). Hence in the Atlantic basin of the modern ocean, transport above b_m is predominantly northward and transport below b_m is predominantly southward.

In our 3D model, a passive tracer C obeys the advection–diffusion equation,

$$\frac{\partial C}{\partial t} + (uC)_x + (vC)_y + (wC)_z = \text{Redi terms} + (\kappa C_z)_z\,, \qquad (6)$$

where

$$\text{Redi terms} = \left[\kappa^{\text{tr}}_{\text{redi}}\left(C_x - \frac{b_x}{b_z}C_z\right)\right]_x + \left[\kappa^{\text{tr}}_{\text{redi}}\left(C_y - \frac{b_y}{b_z}C_z\right)\right]_y + \left[\kappa^{\text{tr}}_{\text{redi}}\left(-\frac{b_x}{b_z}C_x - \frac{b_y}{b_z}C_y + \left|\frac{\nabla_h b}{b_z}\right|^2 C_z\right)\right]_z\,, \qquad (7)$$

and the velocities (u, v, w) are the sum of the resolved Eulerian velocity and the parameterized eddy velocity. For our 1D model, we integrate this equation from the bottom ($z = -H$) to the dividing isopycnal $z = \zeta(b_m)$, move the derivatives outside the integrals, and move to the buoyancy coordinate system $(\tilde t, \tilde x, \tilde y, \tilde z)$ described by Young (2012), to give

$$\left(\int_{-H}^{\zeta(b_m)} C\,dz\right)_{\tilde t} + \left(\int_{-H}^{\zeta(b_m)} uC\,dz\right)_{\tilde x} + \left(\int_{-H}^{\zeta(b_m)} vC\,dz\right)_{\tilde y} + \frac{\varpi}{b_z}C\bigg|_{\zeta(b_m)} = \left(\int_{-H}^{\zeta(b_m)} \kappa^{\text{tr}}_{\text{redi}} C_{\tilde x}\,dz\right)_{\tilde x} + \left(\int_{-H}^{\zeta(b_m)} \kappa^{\text{tr}}_{\text{redi}} C_{\tilde y}\,dz\right)_{\tilde y} + \kappa C_z\big|_{\zeta(b_m)}\,, \qquad (8)$$

where ϖ/b_z is the diapycnal velocity at $z = \zeta(b_m)$. We approximate C to be constant in the vertical direction below b_m: Figs. 7a,c and 8b,e show that this is a good approximation. We also set $h = \zeta(b_m) + H$ and $(U, V) = \int_{-H}^{\zeta(b_m)}(u, v)\,dz$, so

$$(\overline{C}h)_{\tilde t} + (U\overline{C})_{\tilde x} + (V\overline{C})_{\tilde y} + \frac{\varpi}{b_z}C\bigg|_{\zeta(b_m)} = (\kappa^{\text{tr}}_{\text{redi}} h \overline{C}_{\tilde x})_{\tilde x} + (\kappa^{\text{tr}}_{\text{redi}} h \overline{C}_{\tilde y})_{\tilde y} + \kappa C_z\big|_{\zeta(b_m)}\,, \qquad (9)$$

where the overbar indicates a mean in the vertical direction below isopycnal b_m.

We divide the domain into three regions: the Atlantic basin, the Pacific basin, and the channel. We assume that the tracer concentration is approximately zonally uniform in each region. Hence, Eq. (9) can be zonally integrated in each of these regions to give

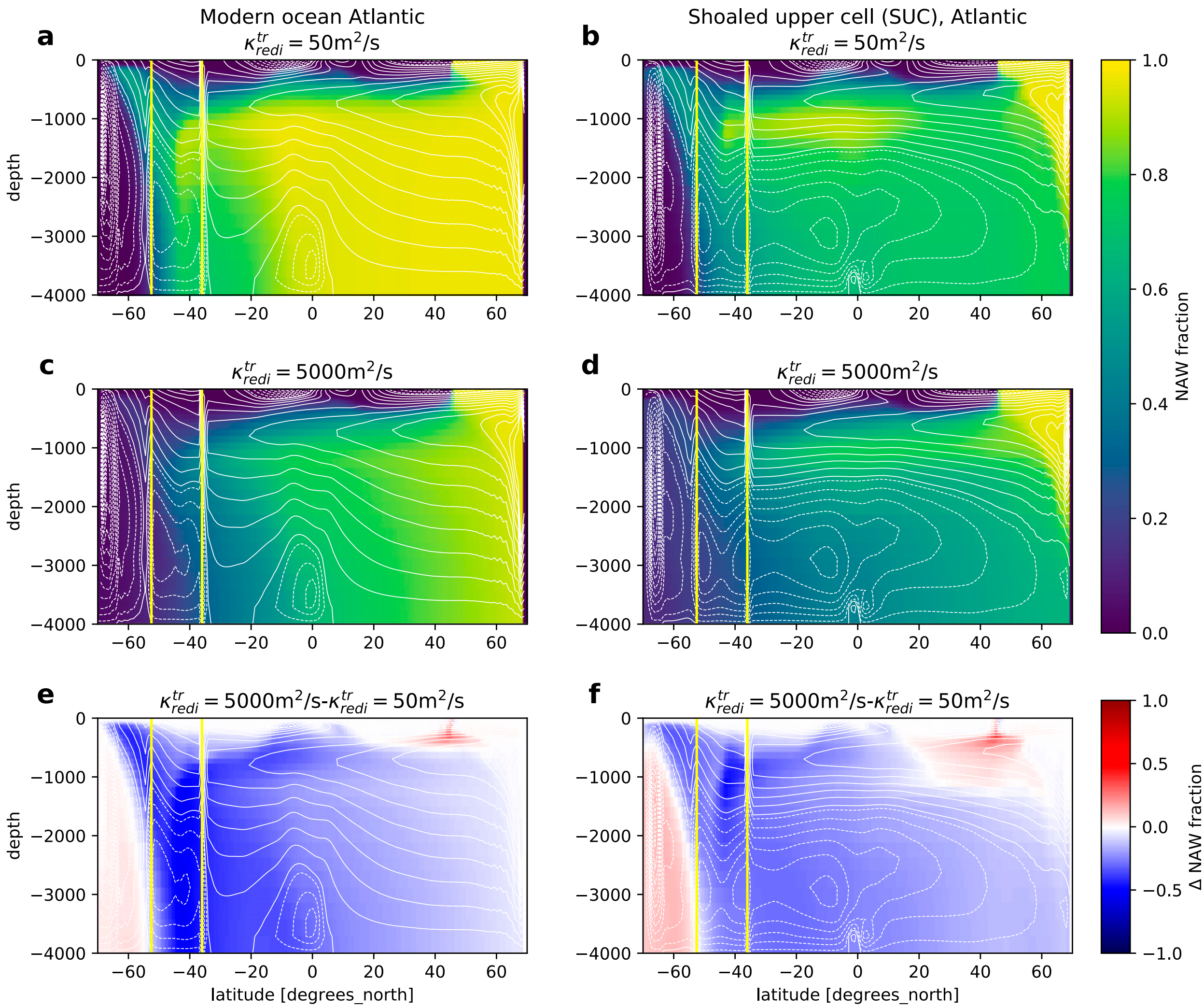

FIG. 7. NAW tracer concentration in the Atlantic basin for uniform isopycnal mixing in (a) the modern ocean with $\kappa^{\mathrm{tr}}_{\mathrm{redi}} = 50\,\mathrm{m}^2\,\mathrm{s}^{-1}$, (b) the shoaled upper cell with $\kappa^{\mathrm{tr}}_{\mathrm{redi}} = 50\,\mathrm{m}^2\,\mathrm{s}^{-1}$, (c) the modern ocean with $\kappa^{\mathrm{tr}}_{\mathrm{redi}} = 5000\,\mathrm{m}^2\,\mathrm{s}^{-1}$, and (d) the shoaled upper cell with $\kappa^{\mathrm{tr}}_{\mathrm{redi}} = 5000\,\mathrm{m}^2\,\mathrm{s}^{-1}$. Also shown is NAW tracer concentration for $\kappa^{\mathrm{tr}}_{\mathrm{redi}} = 5000\,\mathrm{m}^2\,\mathrm{s}^{-1}$ minus $\kappa^{\mathrm{tr}}_{\mathrm{redi}} = 50\,\mathrm{m}^2\,\mathrm{s}^{-1}$ for (e) the modern ocean and (f) the shoaled upper cell. The vertical yellow lines at 35° and 52.5°S indicate where the short and long continents end, respectively. The white contours show the meridional overturning streamfunction calculated in depth space. North of 35°S the streamfunction is calculated for each basin, and south of 35°S it is calculated for the whole zonal extent of the domain.

$$(\overline{C}hL_x)_{\tilde{t}} + (VL_x\overline{C})_{\tilde{y}} + \frac{\varpi}{b_z}L_xC\Big|_{\zeta(b_m)} = (\kappa^{\mathrm{tr}}_{\mathrm{redi}}hL_x\overline{C}_{\tilde{y}})_{\tilde{y}} + L_x\kappa C_z\Big|_{\zeta(b_m)}, \qquad (10)$$

where L_x is the width of the basin or channel. This 1D equation forms the basis of our 1D advection–diffusion model. Inputs to the 1D model are 1) boundary conditions in the North Atlantic, North Pacific, and Southern Ocean; 2) smoothed idealized versions of isopycnal depth $\zeta(b_m)$, shown by the dashed line in the top panel of Fig. 9; 3) smoothed meridional transports, VL_x, which are shown by the dashed lines in the second panel of Fig. 9; and 4) values for L_x, $\kappa^{\mathrm{tr}}_{\mathrm{redi}}$, and κ.

The diapycnal velocity ϖ/b_z is defined using the divergence of the meridional transport. When ϖ/b_z is positive, $C|_{\zeta(b_m)}$ is approximated by the upstream tracer concentration $\overline{C}$. When ϖ/b_z is negative, $C|_{\zeta(b_m)}$ is approximated by the surface tracer concentration C_s. Concentration C_s is set to 1 in the region associated with the chosen tracer and C_s is set to 0 outside this region. The vertical tracer gradient across the isopycnal b_m that is used in the vertical diffusion term in Eq. (10) is approximated by

$$C_z\Big|_{\zeta(b_m)} \approx \frac{C_s - \overline{C}}{h}. \qquad (11)$$

Equation (10) is solved numerically by stepping forward in time until the tracer concentration reaches equilibrium for two different water-mass tracers: the NAW tracer and the AABW

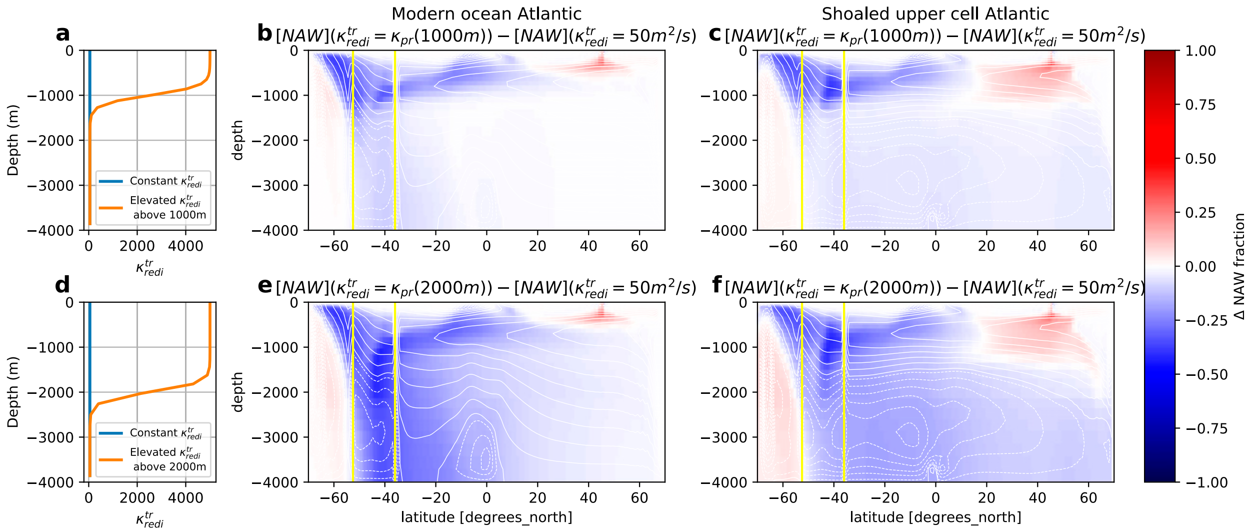

FIG. 8. Isopycnal mixing profile for d = (a) 1000 and (d) 2000 m. Also shown is NAW tracer concentration for $d = 1000$ m minus tracer concentration for $\kappa^{tr}_{redi} = 50\,m^2\,s^{-1}$ in (b) the modern ocean and (c) the shoaled upper cell and for $d = 2000$ m minus tracer concentration for $\kappa^{tr}_{redi} = 50\,m^2\,s^{-1}$ in (e) the modern ocean and (f) the shoaled upper cell.

tracer. These tracers are advected and diffused using identical velocities and isopycnal mixing coefficients, but they have different boundary conditions. For NAW tracer, the boundary conditions are $\overline{C} = 1$ at 70°N in the Atlantic, $\overline{C} = 0$ at 70°S, and $d\overline{C}/dy = 0$ at 70°N in the Pacific. For AABW tracer, the boundary conditions are $\overline{C} = 0$ at 70°N in the Atlantic, $\overline{C} = 1$ at 70°S, and $d\overline{C}/dy = 0$ at 70°N in the Pacific. For NAW tracer, C_s is set to 0 outside the North Atlantic box and is set to 1 inside the North Atlantic box. In both cases the tracer transport at the northern edge of the channel is matched to the transport at the southern edge of each basin at 46°S. The location 46°S is chosen because it is the location of the zero-wind stress-curl line, which approximately divides the eastward flow of the Antarctic Circumpolar Current from the gyres.

b. *Predictions of the 1D model for the modern ocean circulation with uniform isopycnal mixing*

The resulting tracer distributions for $\kappa^{tr}_{redi} = 50\,m^2\,s^{-1}$, $\kappa^{tr}_{redi} = 500\,m^2\,s^{-1}$, and $\kappa^{tr}_{redi} = 5000\,m^2\,s^{-1}$ in the modern ocean are shown in the top two rows of panels in Fig. 10, with the solid lines representing tracer distributions from the 3D model, zonally and depth averaged below b_m, and the dashed lines representing the tracer distributions from the 1D model. For the modern ocean circulation, the model successfully predicts the concentration of NAW tracer and AABW tracer in the deep Atlantic Ocean and in the channel. The 1D model slightly overestimates Pacific NAW concentrations and underestimates Pacific AABW concentrations for low isopycnal mixing, perhaps because meridional velocities that cancel in the zonal and vertical average move NAW to the surface of the Southern Ocean. This transport is too small to be important in regimes with higher isopycnal mixing coefficients.

For the most part, these results validate the assumptions of the 1D model, indicating that tracer concentrations in the deep ocean are set by a combination of the boundary conditions, the meridional velocity (including the parameterized eddy velocity), depth and zonally averaged below b_m, and the isopycnal mixing coefficient, κ^{tr}_{redi}. The effects of diapycnal mixing are negligible in most locations, but act to reduce the concentration of NAW in the deep North Pacific. The results also indicate that vertical variations in tracer transport below b_m and zonal nonuniformities in the meridional velocity do not influence tracer distributions very much. As described in Jones and Abernathey (2019), the main effect of increasing κ^{tr}_{redi} in our modern experiments is a reduction in the amount of NADW in the deep Pacific (cf. black lines in Fig. 10c with Fig. 10a), which is compensated by an increase in AABW in the deep Pacific (cf. black lines in Fig. 10f with Fig. 10d). Increasing κ^{tr}_{redi} also reduces the amount of North Atlantic Water in the deep South Atlantic: again this is compensated by an increase in AABW in this region (cf. red lines in Figs. 10a,d with Figs. 10c,f).

To better understand the mechanisms that determine the tracer concentrations, we examine the different components of the tracer flux. The bottom row of panels in Fig. 10 shows the meridional advective and diffusive transport of North Atlantic Water in the 1D model for $\kappa^{tr}_{redi} = 50\,m^2\,s^{-1}$, $\kappa^{tr}_{redi} = 500\,m^2\,s^{-1}$, and $\kappa^{tr}_{redi} = 5000\,m^2\,s^{-1}$. For the modern overturning circulation, the net volume transport below b_m in the channel is small, with northward transport canceling with southward transport in the abyssal cell, as shown in the left panels of Fig. 2. We represent the volume transport in the channel below b_m in the 1D model as zero for the modern ocean, as shown in the second panel of Fig. 9. As a result, the advective transport in the channel region is zero, as shown in Figs. 10g–i, and diffusive transport controls tracer concentrations in the channel.

For $\kappa^{tr}_{redi} = 50\,m^2\,s^{-1}$ (Fig. 10g), the advective NAW tracer transport dominates the diffusive NAW tracer transport in the Atlantic and Pacific basins (cf. red and black lines in Fig. 10g). In the channel, where the advective NAW tracer transport is zero, there is a small southward diffusive transport of NAW

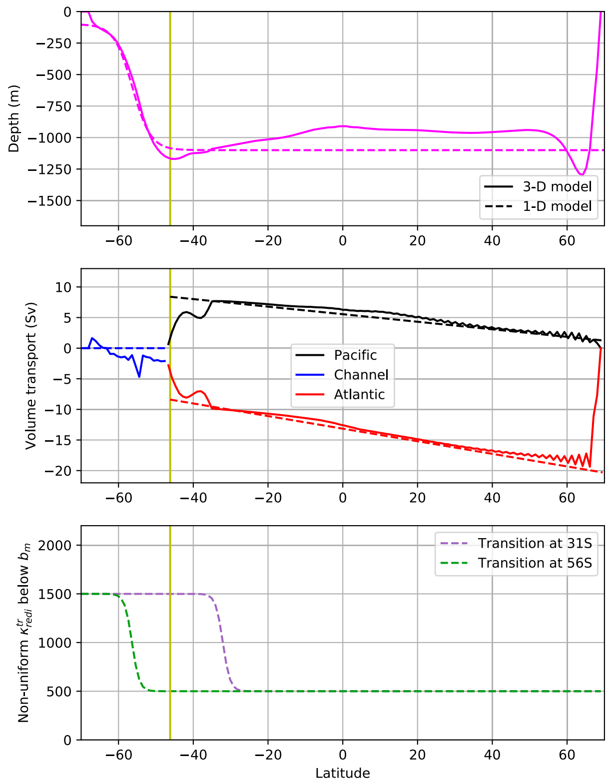

FIG. 9. (top) Depth of isopycnal b_m in the modern ocean for the 3D primitive equation model (solid lines) and the analytical model (dashed lines). (middle) Volume transport below isopycnal b_m in the modern state for the 3D primitive equation model (solid lines) and the analytical model (dashed lines), in the Atlantic (red), Pacific (black), and channel (blue). (bottom) Isopycnal mixing coefficient for the 1D model with meridionally varying isopycnal-mixing coefficient.

tracer (blue dotted line in Fig. 10g). Most of the southward NAW tracer transport in the South Atlantic feeds northward NAW tracer transport in the South Pacific, leading to high NAW tracer concentrations in the deep Pacific (black lines in Fig. 10a). The left part of Fig. 11 summarizes this result: for low isopycnal mixing coefficient, advection moves NAW tracer into the deep Pacific Ocean.

For $\kappa_{\text{redi}}^{\text{tr}} = 500\,\text{m}^2\,\text{s}^{-1}$, advective transport still dominates in the Atlantic and Pacific basins (red and black dashed–dotted lines in Fig. 10h), but about half of the southward advective transport in the Atlantic feeds southward diffusive transport of tracer in the channel (blue dotted line in Fig. 10h): this tracer is destroyed at the surface of the Southern Ocean. For $\kappa_{\text{redi}}^{\text{tr}} = 5000\,\text{m}^2\,\text{s}^{-1}$, diffusive transport dominates over advective transport in the South Atlantic (red dotted line in Fig. 10i), and most NAW tracer is transported to the surface of the Southern Ocean by diffusive transport in the channel. Hence, much less NAW tracer is advected into the deep Pacific (black line in Fig. 10c). Figure 11 illustrates this: when the isopycnal mixing coefficient is increased, isopycnal mixing moves NAW tracer toward the surface of the Southern Ocean, where it is replaced with AABW tracer.

c. *Predictions of the 1D model for the modern ocean circulation with nonuniform isopycnal mixing*

The results above suggest that isopycnal mixing is most important in the upper part of the Southern Ocean, where isopycnals that extend into the deep Atlantic reach the surface. To test this, we looked at how a meridionally varying isopycnal mixing coefficient affects ocean tracer distributions in the 1D model. We chose to change the isopycnal-mixing coefficient by a smaller factor in these experiments to better model possible spatial variations in the magnitude of isopycnal mixing.

Two different distributions of the isopycnal-mixing coefficient are chosen (bottom panel of Fig. 9): one distribution has a larger isopycnal-mixing coefficient south of 31°S and one distribution has a larger isopycnal-mixing coefficient south of 56°S. Both distributions have $\kappa_{\text{redi}}^{\text{tr}} = 500\,\text{m}^2\,\text{s}^{-1}$ throughout most of the basin, and $\kappa_{\text{redi}}^{\text{tr}} = 1500\,\text{m}^2\,\text{s}^{-1}$ in the far south of the Southern Ocean.

When the isopycnal mixing coefficient is increased to $1500\,\text{m}^2\,\text{s}^{-1}$ south of 31°S the amount of NAW tracer reaching the deep Pacific decreases (cf. the black dashed lines in Fig. 12a to Fig. 10b). The NAW tracer concentration in the Atlantic basin is unaffected north of about 31°S (cf. the red dashed lines in Fig. 12a with Fig. 10b). This confirms that the isopycnal-mixing coefficient in the Southern Ocean is a strong control on deep Pacific water-mass concentrations but has a smaller effect on deep North Atlantic water-mass concentrations.

When the isopycnal mixing coefficient is increased to $1500\,\text{m}^2\,\text{s}^{-1}$ south of 56°S, there is a smaller change in NAW tracer concentration in the deep Pacific (cf. the black dashed lines in Fig. 12b to Fig. 10b). This shows that the isopycnal-mixing coefficient must be elevated throughout the Southern Ocean in order to effectively transport NAW to the surface of the Southern Ocean. This result suggests a new mechanism by which changing the position of Southern Ocean winds may influence deep-ocean water-mass distributions.

d. *Predictions of the 1D model for the shoaled upper cell*

The 1D model does not predict SUC tracer concentrations successfully (Fig. 7 in the online supplemental material). In this regime, the assumption that the tracer concentration below b_m is constant in the vertical does not hold (see the top-right panel of Fig. 3). In other words, vertical variations in the velocity below b_m are important for tracer transport by the shoaled-upper-cell circulation.

The 1D model described above was extended to better model tracer transport by the shoaled-upper-cell circulation. An additional layer was added to the model. This extension significantly complicates the 1D model, and it is harder to draw clean mechanistic conclusions from this two-layer version of the model. However, the success of the two-layer version of the model, as described below, confirms that vertical variations in velocity are an important factor in determining deep-ocean tracer concentrations for the shoaled upper cell.

For this two-layer version of the model, the first layer is between b_m and $b = 0.01\,\text{m}^2\,\text{s}^{-1}$, and the second layer is

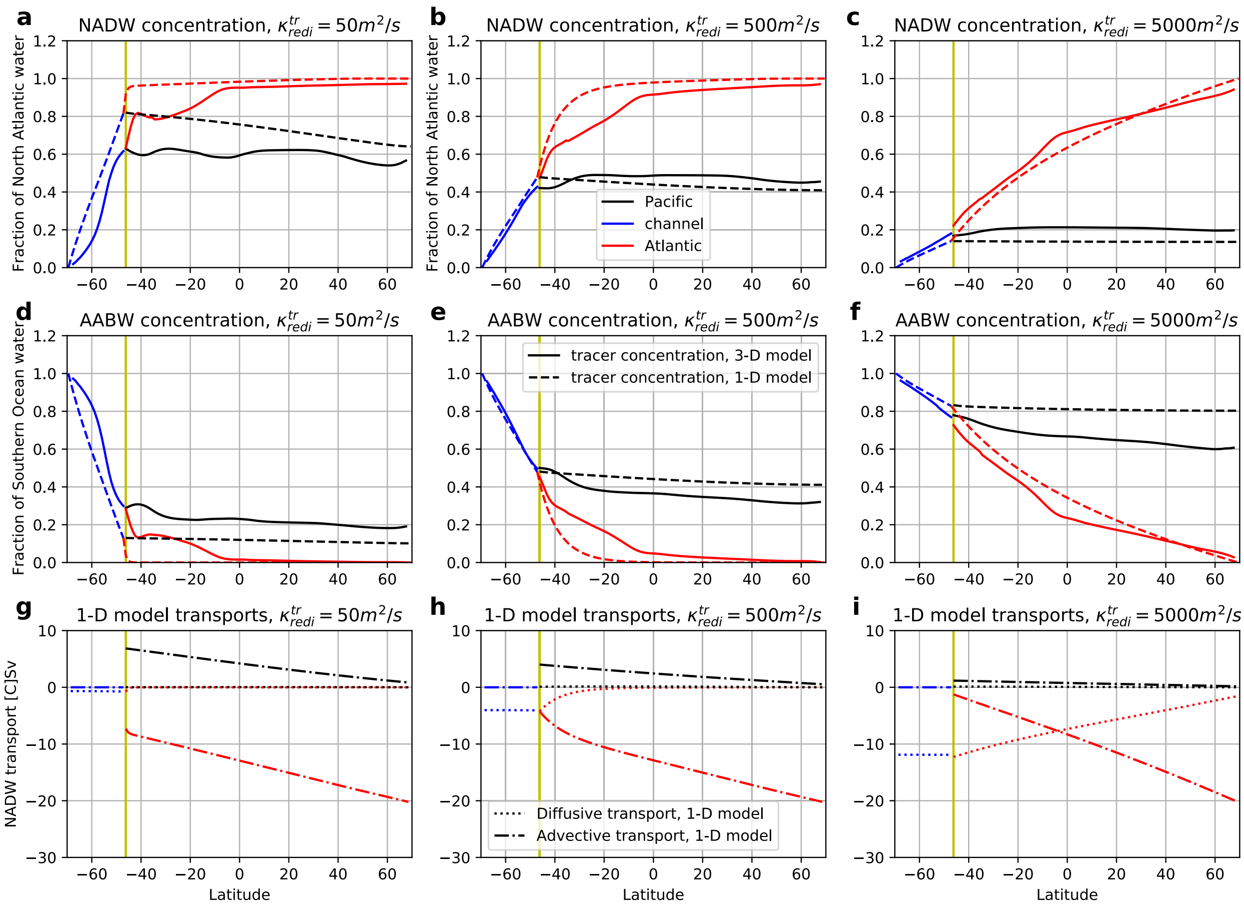

FIG. 10. Concentration of (a)–(c) NAW tracer and (d)–(f) AABW tracer in the 3D model, integrated over each basin and below isopycnal b_m (solid lines), and in the 1D advection–diffusion model (dashed lines). (g)–(i) Meridional advective (dash–dotted lines) and diffusive (dotted lines) transport of NAW tracer in the 1D model.

between the bottom and $b = 0.01\ \mathrm{m^2\,s^{-1}}$; $\overline{C_1}$ is the mean tracer concentration in the layer between b_m and $b = 0.01\ \mathrm{m^2\,s^{-1}}$ and $\overline{C_2}$ is the mean tracer concentration in the layer between the bottom and $b = 0.01\ \mathrm{m^2\,s^{-1}}$. For NAW tracer, the second layer has boundary conditions $\overline{C_2} = 0$ at 70°S and $d\overline{C_2}/dy = 0$ at 70°N. The first layer has the same boundary conditions as before.

The tracer is evolved according to

$$(\overline{C}_1 hL_x)_{\tilde t} + (VL_x\overline{C}_1)_{\tilde y} + \frac{\varpi}{b_z}\bigg|_{\zeta(b_m)} L_x\,\overline{C_{s,1}} - \frac{\varpi}{b_z}\bigg|_{\zeta(b=0.01)} L_x\overline{C_{1,2}} = (\kappa^{\mathrm{tr}}_{\mathrm{redi}} hL_x\overline{C}_{1\tilde y})_{\tilde y} + L_x\kappa C_{1z}\Big|_{\zeta(b_m)} + L_x\kappa C_{1z}\Big|_{\zeta(b=0.01)} \quad \text{and} \tag{12}$$

$$(\overline{C}_2 hL_x)_{\tilde t} + (VL_x\overline{C}_2)_{\tilde y} + \frac{\varpi}{b_z}\bigg|_{\zeta(b=0.01)} L_x\overline{C_{1,2}} = (\kappa^{\mathrm{tr}}_{\mathrm{redi}} hL_x\overline{C}_{2\tilde y})_{\tilde y} + L_x\kappa C_{2z}\Big|_{\zeta(b=0.01)}. \tag{13}$$

where $\overline{C_{s,1}}$ refers to C_s when the surface layer is upstream and $\overline{C_1}$ when layer 1 is upstream and $\overline{C_{1,2}}$ refers to $\overline{C_1}$ when layer 1 is upstream and to $\overline{C_2}$ when layer 2 is upstream.

The vertical diffusion term between the two layers is approximated as

$$L_x\kappa_v C_{1z}\Big|_{\zeta(b=0.01)} \approx \frac{L_x\kappa_v(\overline{C_2} - \overline{C_1})}{\zeta(b=0.01) - \zeta(b_m)} \quad \text{and} \tag{14}$$

$$L_x\kappa_v C_{2z}\Big|_{\zeta(b=0.01)} \approx \frac{L_x\kappa_v(\overline{C_1} - \overline{C_2})}{\zeta(b=0.01) - \zeta(b_m)}. \tag{15}$$

The layer depths and volume transports used in the two-layer version of the 1D model are shown in Fig. 13. In this version of the 1D model, the channel edge is moved to 35°S, where the short continent ends. The isopycnal $b = 0.01\ \mathrm{m^2\,s^{-1}}$, which defines the upper surface of layer 2, reaches the bottom of the ocean just north of 50°N. When $b = 0.01\ \mathrm{m^2\,s^{-1}}$ is within 100 m of the bottom, the vertical diffusion of tracer is reduced to zero. This is a simplification of a real physical effect: the diffusivity decreases toward the bottom of the ocean within the bottom boundary layer (Ferrari et al. 2016).

The resulting tracer distributions are shown in Fig. 14. Overall, the two-layer version of the 1D model performs well for the shoaled upper cell. For small isopycnal diffusivities, the two-layer version of the 1D model predicts deep-ocean tracer concentrations successfully. For large isopycnal diffusivities, the model underestimates the amount of NAW tracer in the

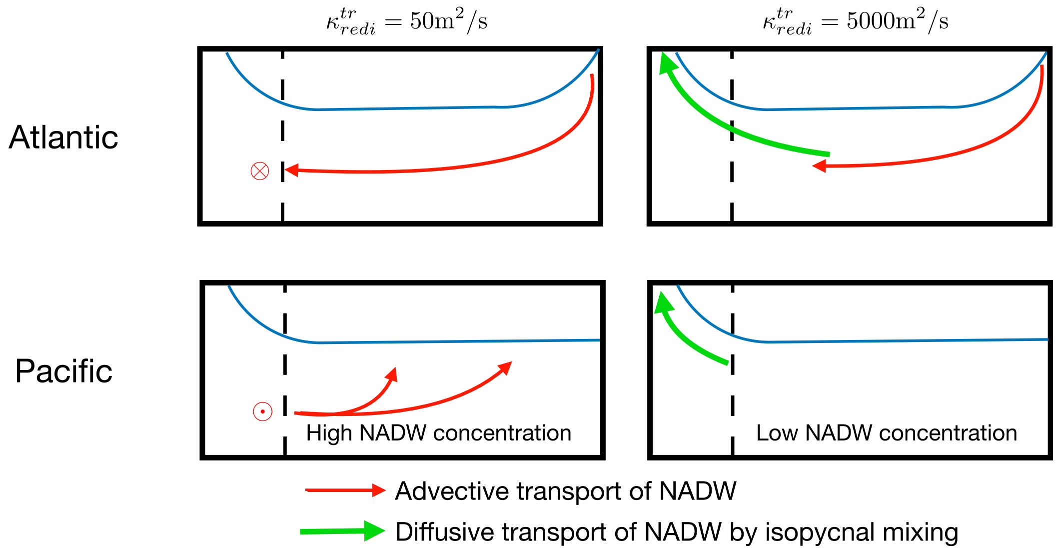

FIG. 11. Schematic of the transport of NADW (left) when isopycnal mixing is small and (right) when it is large.

lower layer, because the southern boundary condition is no longer accurate. Although it is difficult to draw mechanistic conclusions from the two-layer model, its success shows that the same advective–diffusive balance governs the SUC circulation and the modern ocean circulation.

5. Discussion and conclusions

This paper uses a 3D primitive equation model and a 1D advection–diffusion model to examine how tracer distributions in the deep ocean depend on the ocean circulation and on the isopycnal-mixing coefficient. In the 3D model, we compared two states of the ocean circulation, one in which the upper cell reached 4000-m depth (the "modern ocean" circulation), and one in which the upper cell only reached about 2500-m depth in the North Atlantic (the "shoaled upper cell"). We used idealized passive tracers to understand the pathways of water masses through these circulations for various different values of isopycnal mixing. The variable isopycnal mixing was applied to our passive water-mass tracers and not to temperature and salinity in order to distinguish the effects of changes in circulation versus changes in mixing.

Our model does not include sea ice, so North Atlantic Water that reaches the mixed layer of the Southern Ocean is ventilated, and its water-mass tracer values are reset to those of AABW. When the upper cell shoals in our model, significant

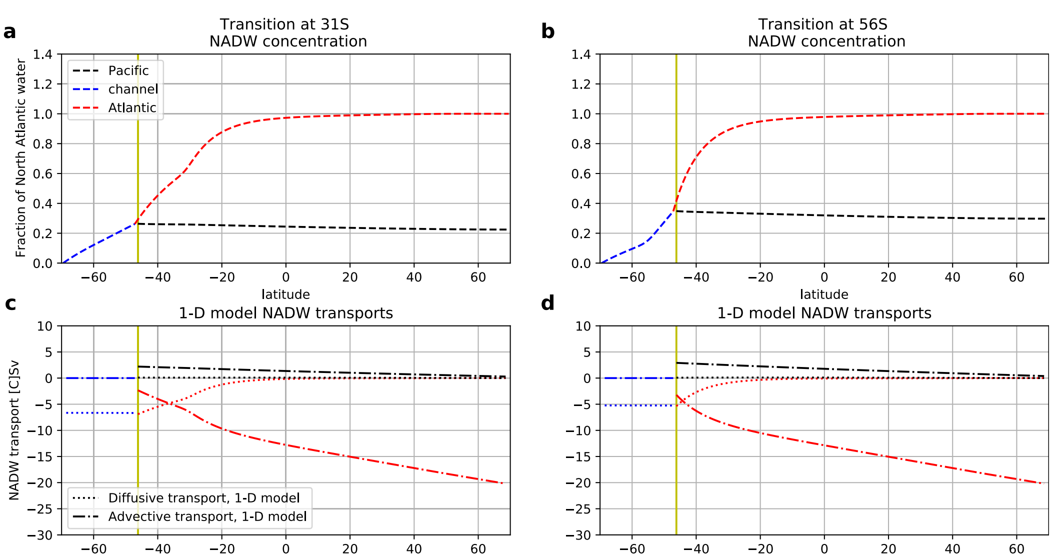

FIG. 12. (a),(b) Concentration of NAW tracer predicted by the one-layer 1D advection–diffusion model. (c),(d) Meridional advective transport of NAW tracer in the 1D model (dash–dotted lines) and meridional diffusive transport of NAW tracer predicted by the 1D advection–diffusion model (dotted lines).

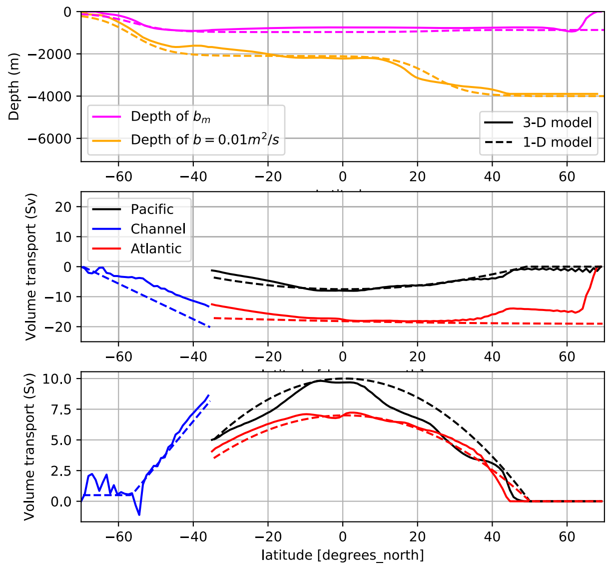

FIG. 13. (top) Depth of the top layer (orange) and the bottom layer (magenta) for the 3D primitive equation model (solid lines) and the analytical model (dashed lines). Also shown is volume transport in the (middle) top and (bottom) bottom layers for the 3D primitive equation model (solid lines) and the two-layer analytical model (dashed lines) in the Atlantic (red), Pacific (black), and channel (blue).

quantities of North Atlantic Water reach the abyssal cell in the Atlantic basin, indicating that there must be an interior pathway for North Atlantic Water to reach the abyssal cell. We find that North Atlantic Water reaches the abyssal cell via interior downwelling throughout the Atlantic basin, due to our chosen profile of vertical diffusivity, which increases with depth (Ferrari et al. 2016). Through this mechanism, North Atlantic Water is entrained into the abyssal cell without first entering the mixed layer in the Southern Hemisphere.

In our 3D model, changing $\kappa_{\mathrm{redi}}^{\mathrm{tr}}$ by a factor of 10 in the upper 2000 m of the ocean has a similar-sized impact on the concentration of North Atlantic Water in the deep Atlantic between the equator and 30°N to shoaling the upper cell (Fig. 4). Abernathey and Ferreira (2015) show that increasing wind over the Southern Ocean causes isopycnal mixing to increase all the way down to 2000-m depth. A factor of 10 increase in isopycnal mixing strength at the LGM is unrealistic, because Southern Ocean winds probably did not increase more than 50% during this period. We conclude that if Southern Ocean winds changed their strength and/or position at the LGM, changes to the strength of isopycnal mixing in the upper ocean may modestly contribute to observed differences in deep-ocean tracer distributions between the modern and LGM oceans. Further research in more realistic models is needed to determine the size of this contribution.

We also developed a 1D model that successfully predicts deep-ocean tracer distributions in the 3D modern experiments. This 1D model elucidates why deep Pacific tracer concentrations are so sensitive to upper ocean isopycnal mixing: when isopycnal-mixing in the Southern Ocean is strong, a large amount of NADW is transported southward by isopycnal mixing in the Southern Ocean, where this NADW is destroyed when it reaches the mixed layer. This strong isopycnal mixing reduces the amount of NADW in the South Atlantic, inhibiting advection of NADW from the South Atlantic into the South Pacific. Hence, increasing the isopycnal mixing coefficient in the Southern Ocean reduces the transport of NADW into the deep North Pacific. In the SUC state, isopycnal mixing transports abyssal NADW southward in both basins.

The 1D model indicates that the strength and extent of isopycnal mixing in the Southern Ocean regulates how much NADW reaches the surface of the Southern Ocean. This

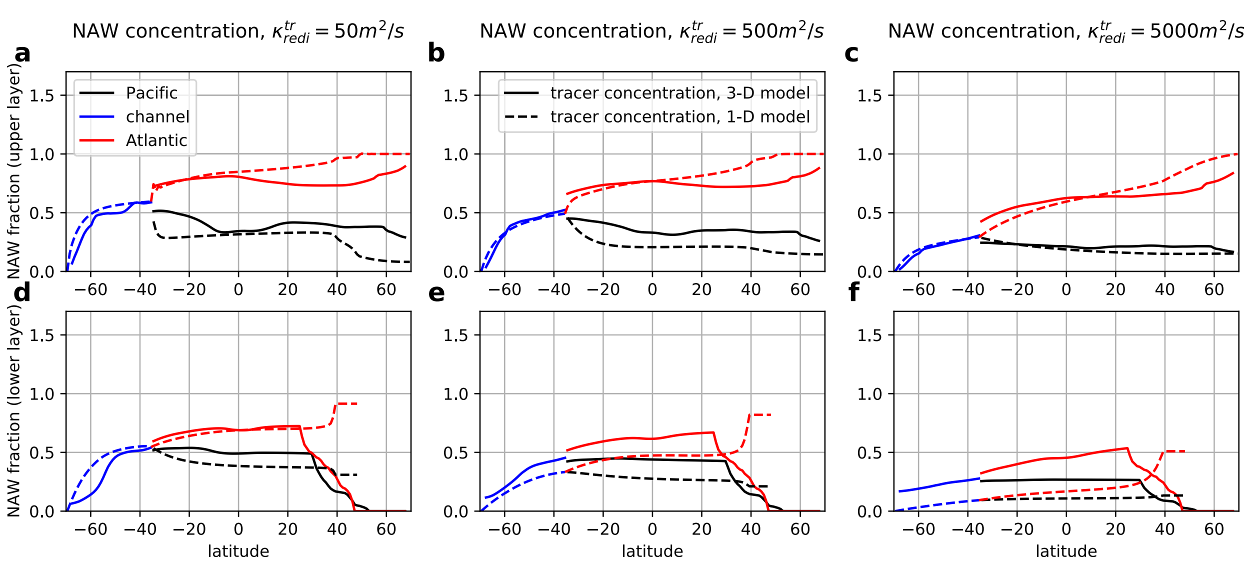

FIG. 14. Concentration of NAW tracer in the 3D model, integrated over each basin (solid lines), and in the 1D advection–diffusion model (dashed lines) in (a)–(c) layer 1 and (d)–(f) layer 2.

suggests that the strength of isopycnal mixing in the Southern Ocean is important for facilitating the exchange of carbon and heat from the mixed layer into the deep ocean. Deep-ocean storage of heat and carbon has a longer time scale than upper ocean storage. More research on the role of isopycnal mixing is needed to explore the ramifications of this finding for future climate predictions.

Acknowledgments. We thank two anonymous reviewers for their extremely helpful comments. Author Jones thanks Sophie Hines and Frank Pavia for many useful conversations about tracer distributions at the LGM and for comments on this paper. Jones is funded by the Lamont Postdoctoral Fellowship. Author Abernathey acknowledges support from NSF Award OCE 1553593. Code is available online (https://github.com/cspencerjones/tracers_LGM), with the data also being available online (http://doi.org/10.6084/m9.figshare.12827579.v1). Xarray (Hoyer and Hamman 2017) and other software tools supported by the Pangeo Project (NSF Award OCE 1740648) were used to perform data analysis and visualization.

REFERENCES

Abernathey, R., and D. Ferreira, 2015: Southern Ocean isopycnal mixing and ventilation changes driven by winds. *Geophys. Res. Lett.*, **42**, 10 357–10 365, https://doi.org/10.1002/2015GL066238.

Adkins, J. F., 2013: The role of deep ocean circulation in setting glacial climates. *Paleoceanography*, **28**, 539–561, https://doi.org/10.1002/palo.20046.

——, K. McIntyre, and D. P. Schrag, 2002: The salinity, temperature, and δ^{18}O of the glacial deep ocean. *Science*, **298**, 1769–1773, https://doi.org/10.1126/science.1076252.

Armi, L., and H. Stommel, 1983: Four views of a portion of the North Atlantic subtropical gyre. *J. Phys. Oceanogr.*, **13**, 828–857, https://doi.org/10.1175/1520-0485(1983)013<0828:FVOAPO>2.0.CO;2.

Burke, A., A. L. Stewart, J. F. Adkins, R. Ferrari, M. F. Jansen, and A. F. Thompson, 2015: The glacial mid-depth radiocarbon bulge and its implications for the overturning circulation. *Paleoceanography*, **30**, 1021–1039, https://doi.org/10.1002/2015PA002778.

Cole, S. T., C. Wortham, E. Kunze, and W. B. Owens, 2015: Eddy stirring and horizontal diffusivity from Argo float observations: Geographic and depth variability. *Geophys. Res. Lett.*, **42**, 3989–3997, https://doi.org/10.1002/2015GL063827.

Curry, W. B., and D. W. Oppo, 2005: Glacial water mass geometry and the distribution of δ^{13}C of σCO_2 in the western Atlantic Ocean. *Paleoceanography*, **20**, PA1017, https://doi.org/10.1029/2004PA001021.

Ferrari, R., M. F. Jansen, J. F. Adkins, A. Burke, A. L. Stewart, and A. F. Thompson, 2014: Antarctic sea ice control on ocean circulation in present and glacial climates. *Proc. Natl. Acad. Sci. USA*, **111**, 8753–8758, https://doi.org/10.1073/pnas.1323922111.

——, A. Mashayek, T. J. McDougall, M. Nikurashin, and J.-M. Campin, 2016: Turning ocean mixing upside down. *J. Phys. Oceanogr.*, **46**, 2239–2261, https://doi.org/10.1175/JPO-D-15-0244.1.

Ferreira, D., J. Marshall, T. Ito, and D. McGee, 2018: Linking glacial-interglacial states to multiple equilibria of climate. *Geophys. Res. Lett.*, **45**, 9160–9170, https://doi.org/10.1029/2018GL077019.

Garabato, A. C. N., D. P. Stevens, A. J. Watson, and W. Roether, 2007: Short-circuiting of the overturning circulation in the Antarctic Circumpolar Current. *Nature*, **447**, 194–197, https://doi.org/10.1038/nature05832.

Gebbie, G., 2014: How much did glacial North Atlantic water shoal? *Paleoceanography*, **29**, 190–209, https://doi.org/10.1002/2013PA002557.

Gent, P. R., and J. C. McWilliams, 1990: Isopycnal mixing in ocean circulation models. *J. Phys. Oceanogr.*, **20**, 150–155, https://doi.org/10.1175/1520-0485(1990)020<0150:IMIOCM>2.0.CO;2.

Gnanadesikan, A., M.-A. Pradal, and R. Abernathey, 2015: Isopycnal mixing by mesoscale eddies significantly impacts oceanic anthropogenic carbon uptake. *Geophys. Res. Lett.*, **42**, 4249–4255, https://doi.org/10.1002/2015GL064100.

Gottschalk, J., and Coauthors, 2019: Mechanisms of millennial-scale atmospheric co2 change in numerical model simulations. *Quat. Sci. Rev.*, **220**, 30–74, https://doi.org/10.1016/j.quascirev.2019.05.013.

Groeskamp, S., B. M. Sloyan, J. D. Zika, and T. J. McDougall, 2017: Mixing inferred from an ocean climatology and surface fluxes. *J. Phys. Oceanogr.*, **47**, 667–687, https://doi.org/10.1175/JPO-D-16-0125.1.

Howe, J. N., A. M. Piotrowski, T. L. Noble, S. Mulitza, C. M. Chiessi, and G. Bayon, 2016: North Atlantic deep water production during the Last Glacial Maximum. *Nat. Commun.*, **7**, 11765, https://doi.org/10.1038/ncomms11765.

Hoyer, S., and J. J. Hamman, 2017: Xarray: N-D labeled arrays and datasets in Python. *J. Open Res. Software*, **5**, 10, https://doi.org/10.5334/jors.148.

Jansen, M. F., and L.-P. Nadeau, 2016: The effect of southern ocean surface buoyancy loss on the deep-ocean circulation and stratification. *J. Phys. Oceanogr.*, **46**, 3455–3470, https://doi.org/10.1175/JPO-D-16-0084.1.

Johnson, G. C., 2008: Quantifying Antarctic Bottom Water and North Atlantic Deep Water volumes. *J. Geophys. Res.*, **113**, C05027, https://doi.org/10.1029/2007JC004477.

Jones, C., and P. Cessi, 2017: Size matters: Another reason why the Atlantic is saltier than the Pacific. *J. Phys. Oceanogr.*, **47**, 2843–2859, https://doi.org/10.1175/JPO-D-17-0075.1.

——, and R. P. Abernathey, 2019: Isopycnal mixing controls deep ocean ventilation. *Geophys. Res. Lett.*, **46**, 13 144–13 151, https://doi.org/10.1029/2019GL085208.

Kamenkovich, I., Z. Garraffo, R. Pennel, and R. A. Fine, 2017: Importance of mesoscale eddies and mean circulation in ventilation of the Southern Ocean. *J. Geophys. Res. Oceans*, **122**, 2724–2741, https://doi.org/10.1002/2016JC012292.

Kim, J.-H., R. R. Schneider, S. Mulitza, and P. J. Müller, 2003: Reconstruction of se trade-wind intensity based on sea-surface temperature gradients in the southeast Atlantic over the last 25 kyr. *Geophys. Res. Lett.*, **30**, 2144, https://doi.org/10.1029/2003GL017557.

Kohfeld, K., R. Graham, A. De Boer, L. Sime, E. Wolff, C. Le Quéré, and L. Bopp, 2013: Southern hemisphere westerly wind changes during the Last Glacial Maximum: Paleo-data synthesis. *Quat. Sci. Rev.*, **68**, 76–95, https://doi.org/10.1016/j.quascirev.2013.01.017.

Kunze, E., 2017a: The internal-wave-driven meridional overturning circulation. *J. Phys. Oceanogr.*, **47**, 2673–2689, https://doi.org/10.1175/JPO-D-16-0142.1.

——, 2017b: Internal-wave-driven mixing: Global geography and budgets. *J. Phys. Oceanogr.*, **47**, 1325–1345, https://doi.org/10.1175/JPO-D-16-0141.1.

Ledwell, J. R., A. J. Watson, and C. S. Law, 1998: Mixing of a tracer in the pycnocline. *J. Geophys. Res.*, **103**, 21 499–21 529, https://doi.org/10.1029/98JC01738.

Lumpkin, R., and K. Speer, 2007: Global ocean meridional overturning. *J. Phys. Oceanogr.*, **37**, 2550–2562, https://doi.org/10.1175/JPO3130.1.

Lund, D., J. Adkins, and R. Ferrari, 2011: Abyssal Atlantic circulation during the Last Glacial Maximum: Constraining the ratio between transport and vertical mixing. *Paleoceanography*, **26**, PA1213, https://doi.org/10.1029/2010PA001938.

Lynch-Stieglitz, J., and Coauthors, 2007: Atlantic meridional overturning circulation during the Last Glacial Maximum. *Science*, **316**, 66–69, https://doi.org/10.1126/science.1137127.

Marshall, J., A. Adcroft, C. Hill, L. Perelman, and C. Heisey, 1997: A finite-volume, incompressible Navier Stokes model for studies of the ocean on parallel computers. *J. Geophys. Res.*, **102**, 5753–5766, https://doi.org/10.1029/96JC02775.

Marzocchi, A., and M. F. Jansen, 2019: Global cooling linked to increased glacial carbon storage via changes in Antarctic sea ice. *Nat. Geosci.*, **12**, 1001–1005, https://doi.org/10.1038/s41561-019-0466-8.

Mashayek, A., H. Salehipour, D. Bouffard, C. Caulfield, R. Ferrari, M. Nikurashin, W. Peltier, and W. Smyth, 2017: Efficiency of turbulent mixing in the abyssal ocean circulation. *Geophys. Res. Lett.*, **44**, 6296–6306, https://doi.org/10.1002/2016GL072452.

Nadeau, L.-P., R. Ferrari, and M. F. Jansen, 2019: Antarctic sea ice control on the depth of North Atlantic deep water. *J. Climate*, **32**, 2537–2551, https://doi.org/10.1175/JCLI-D-18-0519.1.

Nikurashin, M., and R. Ferrari, 2013: Overturning circulation driven by breaking internal waves in the deep ocean. *Geophys. Res. Lett.*, **40**, 3133–3137, https://doi.org/10.1002/grl.50542.

Oppo, D. W., G. Gebbie, K.-F. Huang, W. B. Curry, T. M. Marchitto, and K. R. Pietro, 2018: Data constraints on glacial Atlantic water mass geometry and properties. *Paleoceanogr. Paleoclimatol.*, **33**, 1013–1034, https://doi.org/10.1029/2018PA003408.

Pavia, F. J., R. F. Anderson, P. Pinedo-Gonzalez, M. Q. Fleisher, M. A. Brzezinski, and R. S. Robinson, 2020: Isopycnal transport and scavenging of ^{230}Th and ^{231}Pa in the Pacific Southern Ocean. *Global Biogeochem. Cycles*, **34**, e2020GB006760, https://doi.org/10.1029/2020GB006760.

Ragen, S., M.-A. Pradal, and A. Gnanadesikan, 2020: The impact of parameterized lateral mixing on the Antarctic Circumpolar Current in a coupled climate model. *J. Phys. Oceanogr.*, **50**, 965–982, https://doi.org/10.1175/JPO-D-19-0249.1.

Redi, M. H., 1982: Oceanic isopycnal mixing by coordinate rotation. *J. Phys. Oceanogr.*, **12**, 1154–1158, https://doi.org/10.1175/1520-0485(1982)012<1154:OIMBCR>2.0.CO;2.

Roach, C. J., D. Balwada, and K. Speer, 2018: Global observations of horizontal mixing from Argo float and surface drifter trajectories. *J. Geophys. Res. Oceans*, **123**, 4560–4575, https://doi.org/10.1029/2018JC013750.

Rojas, M., 2013: Sensitivity of southern hemisphere circulation to LGM and 4× CO_2 climates. *Geophys. Res. Lett.*, **40**, 965–970, https://doi.org/10.1002/grl.50195.

Rudnickas, D., Jr., J. Palter, D. Hebert, and H. T. Rossby, 2019: Isopycnal mixing in the North Atlantic oxygen minimum zone revealed by RAFOS floats. *J. Geophys. Res. Oceans*, **124**, 6478–6497, https://doi.org/10.1029/2019JC015148.

Sime, L. C., K. E. Kohfeld, C. Le Quéré, E. W. Wolff, A. M. de Boer, R. M. Graham, and L. Bopp, 2013: Southern hemisphere westerly wind changes during the Last Glacial Maximum: Model-data comparison. *Quat. Sci. Rev.*, **64**, 104–120, https://doi.org/10.1016/j.quascirev.2012.12.008.

——, D. Hodgson, T. J. Bracegirdle, C. Allen, B. Perren, S. Roberts, and A. M. de Boer, 2016: Sea ice led to poleward-shifted winds at the Last Glacial Maximum: The influence of state dependency on CMIP5 and PMIP3 models. *Climate Past*, **12**, 2241–2253, https://doi.org/10.5194/cp-12-2241-2016.

Stephens, B. B., and R. F. Keeling, 2000: The influence of Antarctic sea ice on glacial–interglacial CO_2 variations. *Nature*, **404**, 171–174, https://doi.org/10.1038/35004556.

St. Laurent, L., A. C. Naveira Garabato, J. R. Ledwell, A. M. Thurnherr, J. M. Toole, and A. J. Watson, 2012: Turbulence and diapycnal mixing in Drake Passage. *J. Phys. Oceanogr.*, **42**, 2143–2152, https://doi.org/10.1175/JPO-D-12-027.1.

Stuut, J.-B. W., M. A. Prins, R. R. Schneider, G. J. Weltje, J. F. Jansen, and G. Postma, 2002: A 300-kyr record of aridity and wind strength in southwestern Africa: Inferences from grain-size distributions of sediments on Walvis Ridge, SE Atlantic. *Mar. Geol.*, **180**, 221–233, https://doi.org/10.1016/S0025-3227(01)00215-8.

Sun, S. I. Eisenman, and A. L. Stewart, 2018: Does Southern Ocean surface forcing shape the global ocean overturning circulation? *Geophys. Res. Lett.*, **45**, 2413–2423, https://doi.org/10.1002/2017GL076437.

Talley, L. D., 2013: Closure of the global overturning circulation through the Indian, Pacific, and Southern Oceans: Schematics and transports. *Oceanography*, **26**, 80–97, https://doi.org/10.5670/oceanog.2013.07.

Trossman, D., L. Thompson, S. Mecking, and M. Warner, 2012: On the formation, ventilation, and erosion of mode waters in the North Atlantic and Southern Oceans. *J. Geophys. Res.*, **117**, C09026, https://doi.org/10.1029/2012JC008090.

Tulloch, R., and Coauthors, 2014: Direct estimate of lateral eddy diffusivity upstream of drake passage. *J. Phys. Oceanogr.*, **44**, 2593–2616, https://doi.org/10.1175/JPO-D-13-0120.1.

Waterhouse, A. F., and Coauthors, 2014: Global patterns of diapycnal mixing from measurements of the turbulent dissipation rate. *J. Phys. Oceanogr.*, **44**, 1854–1872, https://doi.org/10.1175/JPO-D-13-0104.1.

Waterman, S., A. C. Naveira Garabato, and K. L. Polzin, 2013: Internal waves and turbulence in the Antarctic circumpolar current. *J. Phys. Oceanogr.*, **43**, 259–282, https://doi.org/10.1175/JPO-D-11-0194.1.

Watson, A. J., G. K. Vallis, and M. Nikurashin, 2015: Southern Ocean buoyancy forcing of ocean ventilation and glacial atmospheric CO_2. *Nat. Geosci.*, **8**, 861–864, https://doi.org/10.1038/ngeo2538.

Wilmes, S.-B., A. Schmittner, and J. M. Green, 2019: Glacial ice sheet extent effects on modeled tidal mixing and the global overturning circulation. *Paleoceanogr. Paleoclimatol.*, **34**, 1437–1454, https://doi.org/10.1029/2019PA003644.

Young, W. R., 2012: An exact thickness-weighted average formulation of the Boussinesq equations. *J. Phys. Oceanogr.*, **42**, 692–707, https://doi.org/10.1175/JPO-D-11-0102.1.